Acta Materialia xxx (xxxx) 118990

Contents lists available at ScienceDirect

Acta Materialia

journal homepage: www.elsevier.com/locate/actamat

Full length article

Correlation between cation order/disorder and the electrocaloric effect in the MLCCs of complex perovskite ferroelectrics

Yongke Yan [a], Liwei D. Geng [b], Li-Qian Cheng [a], Xiaotian Li [a], Haoyang Leng [a], Ke Wang [c], Bed Poudel [a], Amin Nozariasbmarz [a], Mohan Sanghadasa [e], Susan Trolier-McKinstry [a, c, d], Qi-Ming Zhang [c, d], Yu U. Wang [b], Shashank Priya [a, *]

[a] Department of Materials Science and Engineering, Pennsylvania State University, University Park, PA 16802, USA
[b] Department of Materials Science and Engineering, Michigan Technological University, Houghton, MI 49931, USA
[c] Materials Research Institute, Pennsylvania State University, University Park, PA 16802, USA
[d] School of Electrical Engineering and Computer Science, Pennsylvania State University, University Park, PA 16802, USA
[e] U.S. Army Combat Capabilities Development Command Aviation & Missile Center, Redstone Arsenal, Alabama 35898, USA

ARTICLE INFO

Article history:
Received 20 October 2022
Received in revised form 26 April 2023
Accepted 6 May 2023

Keywords:
Electrocalorics
Complex perovskite ferroelectrics
Disorder
Multi-layer ceramic capacitors

ABSTRACT

The physical properties (dielectric, ferroelectric, piezoelectric, etc.) of complex perovskite ferroelectrics depend on the degree of order/disorder and the scale of the ordered domains. In this study, the electrocaloric (EC) properties of three representative complex perovskite ferroelectrics, $Pb(Mg_{1/3}Nb_{2/3})O_3$–$8PbTiO_3$ (PMN-8PT), 1mol% Sm-doped $Pb(Mg_{1/3}Nb_{2/3})O_3$–$8PbTiO_3$ (1S-PMN-8PT) and $Pb(Sc_{1/2}Ta_{1/2})O_3$ (PST) are evaluated. Multi-layer ceramic capacitors (MLCCs) with identical structural configurations were fabricated for these three compounds, and their EC properties were characterized by direct measurement using a thermocouple. The EC temperature change ΔT of PMN-8PT, 1S-PMN-8PT and PST MLCCs under 20 V μm^{-1} at room temperature were found to be 1.42 K, 1.54 K, and 3.10 K, respectively. X-ray diffraction and high-resolution transmission electron microscopy data suggests that the high EC performance of PST is related to the ordering of B-site cations (Sc^{3+} and Ta^{5+}) with the ordering parameter $S = 0.82$ and a long coherence length of ~100 nm, such that the sample transitioned from a relaxor ferroelectric to a normal ferroelectric. These results provide pathway towards design of high performance EC materials required for solid state refrigeration and air-conditioning technologies.

1. Introduction

The electrocaloric effect (ECE) is an electric field-induced isothermal entropy change ΔS and adiabatic temperature change ΔT in dielectric materials [1–3]. Refrigeration based on the ECE generates zero greenhouse gas emission and has the promise of achieving higher efficiency, compared with the present vapor compression cycle (VCC) based refrigeration. Moreover, EC cooling is both solid-state and compressor-free, which has advantages of scalability, compact size, and voltage-driven operation as compared to other solid-state cooling technologies [2]. Owing to these advantages, thin film EC materials are also being pursued for on-chip cooling.

Ferroelectrics have been demonstrated to exhibit ECE in single crystals, bulk ceramics, thick film, thin films, polymers, and composites [1,2,4]. To generate a large ECE, typically an electric field of 10–100 V μm^{-1} is required [1,2]. Hence, the ECE-generated ΔT tends to be small in bulk materials due to the required high driving voltage and low breakdown electric fields. In contrast, thin films can withstand large electric fields and therefore exhibit larger ECE, [5,6] but have limited heat sinking capacity owing to their small thickness (< 3 μm) and/or low volume. Multilayer structure with EC thick films and interdigitated metallic inner electrodes (Pt, Ag, Ni, etc.) increase the total volume while maintaining lower driving voltage and high EC values [7]. EC multi-layer ceramic capacitors (EC MLCCs) are highly reliable and have the potential of generating high ECE, and thus are appealing to study the EC behavior in different material compositions.

For large ECE, there is a particular interest in B-site complex perovskite ferroelectrics, such as $Pb(Mg_{1/3}Nb_{2/3})O_3$ (abbreviated as PMN) and $Pb(Sc_{1/2}Ta_{1/2})O_3$ (abbreviated as PST) [8–10]. Both PMN and PST have been fabricated into EC MLCCs, and their EC performance have been reported [8–10]. $0.92Pb(Mg_{1/3}Nb_{2/3})O_3$–$0.08PbTiO_3$ (PMN-8PT) EC-MLCCs give a maximum electrocaloric temperature change of $\Delta T = 2.67$ K at 80 °C for an electric field excursion of $\Delta E = 16$ V μm^{-1} [9] $0.9Pb(Mg_{1/3}Nb_{2/3})O_3$–$0.1PbTiO_3$ EC-MLCCs have a peak electrocaloric temperature change of $\Delta T = 2.7$ K at 107 °C for an electric field excursion of $\Delta E = 28.8$ V μm^{-1} [10]. For $Pb(Sc_{1/2}Ta_{1/2})O_3$ (PST) composition, EC-MLCCs with high B-site ordering have been reported, which generate a peak $\Delta T = 5.5$ K near room temperature under 29 V

* Corresponding author.
E-mail address: sup103@psu.edu (S. Priya).

https://doi.org/10.1016/j.actamat.2023.118990
1359-6454/© 20XX

μm^{-1}, representing the state-of-art in MLCCs [8]. To demonstrate the cooling power and temperature span, PST MLCCs with lower EC ΔT were employed in two different EC cooling devices. In those two studies, the EC ΔT is 2.3 K at 38 °C under 15.8 V μm^{-1} and EC ΔT is 2.5 K at room temperature under 10.8 V μm^{-1} [11,12]. Overall, PST MLCCs have larger ECE than PMN-based MLCCs near room temperature.

It is well known that the reported EC ΔT vary widely due, in part, to different measurement approaches [13]. For example, the widely used indirect thermodynamic method based on the Maxwell relation, may not be applicable especially for non-ergodic relaxor ferroelectrics [13]. Therefore, direct measurement of different materials on a single measurement system is important to understand the changes in electrocaloric performance.

$Pb(Mg_{1/3}Nb_{2/3})O_3$ and $Pb(Sc_{1/2}Ta_{1/2})O_3$ are two representative B-site complex perovskite ferroelectrics considered for this study. The relaxor behavior originates from short-range ordering in the arrangement of different ions on the B-sites. The electrostatic and elastic energies of the structure due to the difference in both the charge and the size of B' and B'' ions promotes ordering, while entropy favors disorder above a certain temperature [14,15]. The types of cations and heat treatment could modify the ordering parameter and thus modulate the size and density of local polar nano regions, this can further alter the phase transition behavior (first order or second order) and ECE performance [16–20]. Therefore, it is interesting to investigate the effect of ordering/disordering on the electrocaloric effect in complex perovskite ferroelectrics.

In this study, $Pb(Mg_{1/3}Nb_{2/3})O_3$–$8PbTiO_3$ (PMN-8PT), 1mol% Sm-doped $Pb(Mg_{1/3}Nb_{2/3})O_3$–$8PbTiO_3$ (1S-PMN-8PT) and $Pb(Sc_{1/2}Ta_{1/2})O_3$ (PST), which have similar temperatures of maximum dielectric susceptibility (T_m), were selected for excluding the effect of temperature range. PMN-8PT, 1S-PMN-8PT and PST MLCCs with identical structural configuration were fabricated and then the EC properties were characterized using the same direct measurement method. X-ray diffraction (XRD) and high-resolution transmission electron microscopy (TEM) were employed to characterize disorder and order in the PMN-8PT and PST. Theoretical analysis was conducted to understand the role of structure and ordering on the EC performance.

2. Experimental procedure

MLCC fabrication: In this study, three compositions were studied: (1) $0.92Pb(Mg_{1/3}Nb_{2/3})O_3$–$0.08PbTiO_3$ (PMN-8PT), (2) 1mol% Sm doped $0.92Pb(Mg_{1/3}Nb_{2/3})O_3$–$0.08PbTiO_3$ (1S-PMN-8PT) and (3) $Pb(Sc_{1/2}Ta_{1/2})O_3$ (PST). Stoichiometric ceramic powders were prepared via the conventional solid-state reaction method, using raw oxides of PbO, $MgNb_2O_6$, TiO_2, Sm_2O_3. Sc_2O_3, and Ta_2O_5. The calcination temperature for PMN-8PT, 1S-PMN-8PT and PST are 750 °C for 2 h, 800 °C for 2 h, 850 °C for 4, respectively. To fabricate MLCCs, the calcined powders were mixed with 45 wt% of an organic binder (B73225, Ferro Corp., USA), 15 wt% toluene/ethanol solvent, and 1 wt% excess PbO to obtain homogenous slurries. The slurry was vacuum defoamed and then tape-cast with a blade height of 200 μm. Pt electrode paste (5574, Electro-Science Laboratories, Inc., USA) was screen-printed on the ceramic tapes. The electroded tapes were stacked to form MLCCs, and the design of the structures is illustrated in Fig. 1a. The stacked samples were warm isostatically pressed at 75 °C and 20 MPa, and then diced into small chips. The binder in the samples was removed by heating to 400 °C at a rate of 0.5 °C/min. PMN-8PT and 1S-PMN-8PT MLCCs were sintered at 1200 °C for 2 h in an O_2 atmosphere. PST MLCCs were sintered at 1300 °C for 2 h in air. Lastly, both sides of the sintered MLCCs were coated with silver paste (7713, DuPont, USA) as electrical terminals, and fired at 550 °C for 30 min.

Characterization: The crystallographic phase and microstructures of ceramics were characterized using X-ray diffraction (XRD, PANalytical Empyrean) and field-emission scanning electron microscopy (FESEM, Apreo) in combination with energy dispersive spectroscopy (EDS). The high-resolution tranmission electron microscopy (HRTEM) images were obtained using an FEI Titan^3 G2 double aberration-corrected microscope at 300 kV. The scanning transmission electron microscopy (STEM) images were collected by using a high-angle annular dark field (HAADF) detector which had a collection angle of 52–253 mrad. The TEM sample was prepared by a focused ion beam (FIB, FEI Helios 660) lift-out technique.

Electrical measurement: The dielectric properties of MLCCs were measured as a function of temperature with a multi-frequency LCR meter (Keysight E4980AL). The polarization vs. electric field hystere-

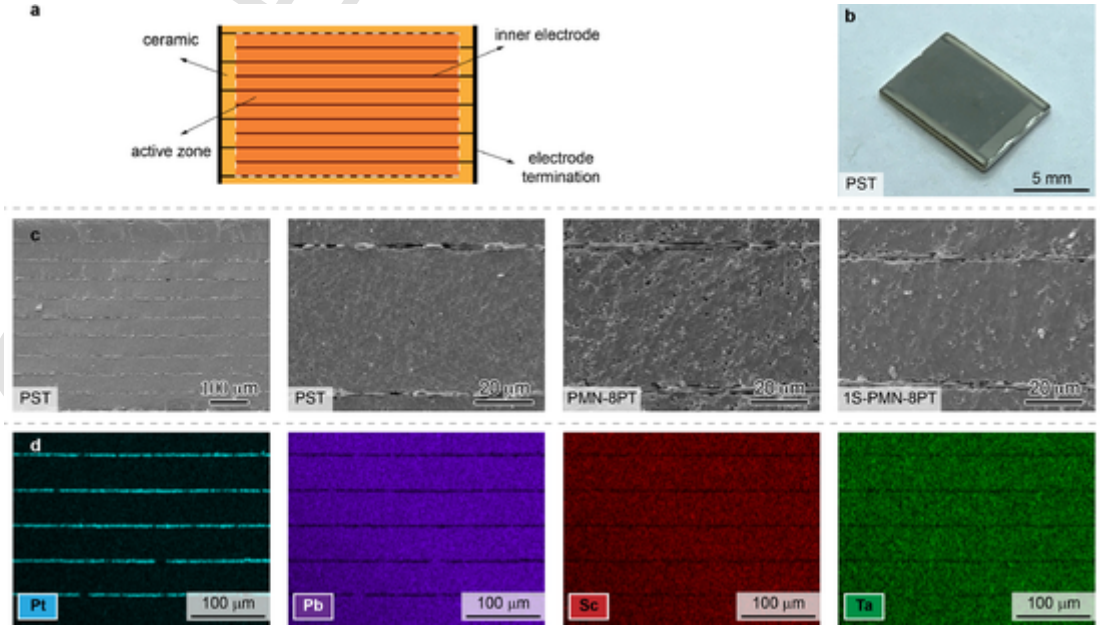

Fig. 1. Microstructures of MLCCs. (a) Schematic cross-sectional structure of an EC-MLCC. (b) Photograph of a PST MLCC. (c) Cross-sectional SEM images of PST, PMN-8PT and 1S-PMN-8PT ceramics. (d) SEM-EDS elemental mapping of PST.

sis loops were measured using a ferroelectric tester (Precision Premier II, Radiant Technologies, Inc., USA). The direct electrocaloric temperature change was measured using a K-type thermocouple with a wire thickness of 50 μm attached directly on the face center of the MLCCs using Kapton tape. The electric field was applied by a wave form generator (33600A, Keysight, USA) and a power amplifier (609B, TREK, USA). The EC temperature change was recorded through a data acquisition software (9210, NI, USA).

3. Results and discussion

3.1. Microstructures of MLCCs

Fig. 1a schematically depicts the structure of an EC-MLCC. There are ten layers of active ceramics with one layer of inactive ceramic on the top and bottom surfaces. The thickness of the inactive ceramic single layer is half of that of the active ceramic single layer. Fig. 1b shows the picture of a PST MLCC. The dimensions of all sintered MLCCs (PMN-8PT, 1S-PMN-8PT and PST) are approximately 9.0 mm in length, 6.0 mm in width and 0.5 mm in thickness. The active volume ratio is 53%. All three types of samples (PMN-8PT, 1S-PMN-8PT and PST) have the same structural configurations except that the layer thickness of ceramics has a slight difference (Fig. 1c) mainly due to the slightly difference of dry green ceramic tapes for different compositions due to the variation of slurry viscosity. Fig. 1c shows the cross-sectional SEM images of MLCCs. All samples show high density and similar grain size (1~2 μm). The relative densities of PMN-8PT MLCCs and PST are estimated to be >97%. The density of 1S-PMN-8PT MLCCs is estimated to be over 99% based on the high transparency of sintered ceramic samples. Rare-earth doping and oxygen sintering atmosphere are widely adopted to fabricate high-density transparent electro-optic PMN-PT ceramics [21]. The thicknesses of each active ceramic layer for all samples are around 45 μm and that of Pt electrode is 2 μm. Fig. 1d shows the SEM-EDS mappings of a PST MLCC. The PST ceramic has uniform composition distribution, and the interface between the PST ceramic and the Pt electrode is sharp.

3.2. Dielectric and ferroelectric properties

Fig. 2a shows the temperature dependence of the dielectric constant for PMN-8PT, 1S-PMN-8PT and PST MLCCs measured at 1 kHz. The temperature T_m for maximum dielectric constant of PMN-8PT, 1S-PMN-8PT and PST MLCCs are found to be 31 ˚C, 4 ˚C, and 14 ˚C, respectively. Sm^{3+} dopant was mainly used for tuning the T_m of PMN-8PT. Here, the 1mol% Sm^{3+} dopant lowers the T_m of PMN-PT by 27 ˚C, which is close to the reported decrease of 25 ˚C per mol% if the rare-earth cation R^{3+} dopant goes on the A site of Pb-based perovskites [22]. The maximum dielectric constant ε_m of PST MLCCs at the T_m is about three times lower than PMN-PT MLCCs and shows a less diffuse permittivity peak. Stenger et al. observed that the permittivity- temperature curves can be modulated by heat treatment by changing the ordering of Sc^{3+} and Ta^{5+} [23]. With the increase in order, the $\varepsilon_{r,\ max}$ decreases while T_m increases. Meanwhile, the permittivity curves sharpen, indicating the transition from relaxor ferroelectrics to normal ferroelectrics. A modified Curie–Weiss law was used to measure the degree of the diffused phased transition (DPT),

$$\frac{1}{\varepsilon} - \frac{1}{\varepsilon_m} = \frac{(T - T_m)^\gamma}{C}, \quad (1)$$

where γ is the diffuseness exponent ($1 \le \gamma \le 2$), C is Curie-Weiss constant. As shown in Fig. 2b, linear fitting between $\ln(1/\varepsilon - 1/\varepsilon_m)$ and $\ln(T\text{-}T_m)$ is applied, and the slope (γ) for PMN-8PT, 1S-PMN-8PT and PST is found to be 1.85, 1.65, and 1.22, respectively, suggesting that PMN-8PT has strongest relaxor behavior and PST has weakest relaxor behavior. The reduced relaxor behavior of PST is due to the formation of high B-cation order during sintering, as will discussed later. Fig. 2c shows the dielectric loss tangents of PMN-8PT, 1S-PMN-8PT and PST MLCCs. At the room temperature, the dielectric loss tangents of PMN-8PT, 1S-

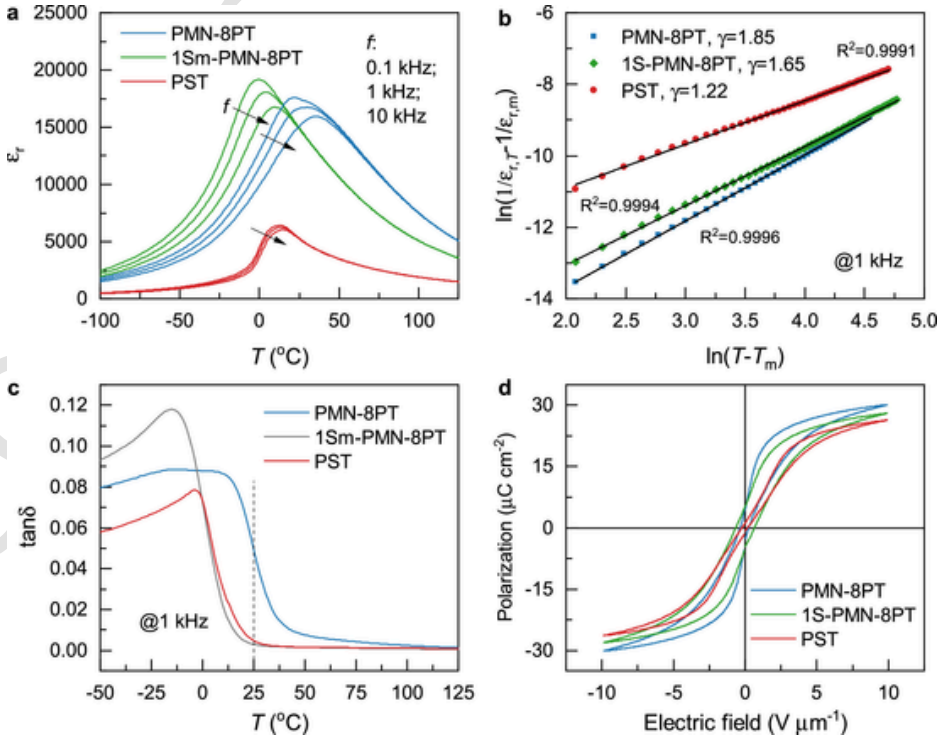

Fig. 2. Temperature dependence of (a) dielectric constant, ε_r for PMN-8PT, 1S-PMN-8PT and PST MLCCs. Temperature dependence of dielectric loss is provided in the discussion section; (b) The plots (symbols) and linear fitting curves (solid line) of $\ln(1/\varepsilon_r\text{-}1/\varepsilon_m)$ as a function of $\ln(T\text{-}T_m)$. (c) Temperature dependent dielectric losses of PMN-8PT, 1S-PMN-8PT and PST MLCCs. (d) Polarization-electric field loops for PMN-8PT, 1S-PMN-8PT and PST MLCCs.

PMN-8PT and PST MLCCs are 4.9%, 0.3%, and 0.5%, respectively. In general, the dielectric loss in ferroelectric materials is mainly due to domain wall motion or motion of the boundaries of micropolar regions [24,25]. As the temperature approaches T_{max}, this motion is enhanced, eventually resulting in higher loss. Fig. 2d shows the polarization-electric field loops for PMN-8PT, 1S-PMN-8PT and PST at room temperature. Comparatively, PST has slightly lower saturation polarization and lower coercive field than PMN-8PT.

3.3. Electrocaloric properties

Fig. 3a presents a typical EC temperature change curve at room temperature under an electric field excitation of a square waveform. The thermocouple attached at the face center recorded the temperature change on field application. The application of an electric field leads to an exothermic temperature rise, and the removal of the field leads to an endothermic temperature drop. The EC temperature change ΔT was recorded under decreasing electric fields. The rise/fall time was 0.125 s. With an excitation electric field of 15 V μm^{-1}, an EC temperature change ΔT of 2.73 K can be achieved in PST MLCCs. This value is similar to the reported numbers (2.3 K at 38 °C under 15.8 V μm^{-1} in ref [10], and 2.5 K at room temperature under 10.8 V μm^{-1} in ref [11]), [11,12] which confirms the reliability of the fabrication process of MLCCs and EC measurements in this study. For the same sample preparation and measurement procedure, the EC performance of PST, PMN-8PT and 1S-PMN-8PT was characterized and compared. Fig. 3b shows the adiabatic EC temperature change ΔT of PMN-8PT, 1S-PMN-8PT and PST MLCCs under different electric fields at room temperature. The EC temperature change ΔT of all samples increases with an increase in the electric field; the EC temperature changes ΔT of PMN-8PT, 1S-PMN-8PT and PST MLCCs under 20 V μm^{-1} are 1.42 K, 1.54 K, and 3.10 K, respectively (with a repeatability of ±0.01 K on multiple measurements).

Fig. 3c shows the adiabatic EC temperature change ΔT of PMN-8PT, 1S-PMN-8PT and PST MLCCs at different temperatures. Under an electric field of 10 V μm^{-1}, the EC temperature change ΔT of PST has a peak value of 2.5 K at 35 °C, while PMN-PT and 1S-PMN-PT have similar peak values of 1.2 K at about 90 °C. Although Sm^{3+} reduces the T_m of PMN-8PT by 27 °C, the EC property of PMN-8PT and 1S-PMN-8PT are similar. The PST has a much higher ECE than PMN-8PT and 1S-PMN-8PT, but the EC temperature change ΔT of PST has a relatively stronger temperature dependence. An increase of the applied electric field leads to a broader peak of ΔT and the temperature of the maximum EC temperature change ΔT shifts toward higher temperatures, which is consistent with the results from previous report [8]. Nair et al. reported that the ΔT of PST driven by an electric field of 29.0 V μm^{-1} exceed 3 K for starting temperatures that span 176 K [8]. Fig. 4a and 4b show the EC data of PMN-8PT, 1S-PMN-8PT and PST MLCCs for different electric fields. It can be observed that for 15 V μm^{-1}, only PMN-8PT MLCCs cannot return to the starting temperature within 120 s. The temperature of PMN-8PT MLCCs starts to increase after 50 s due to Joule heating.

3.4. Cation order/disorder in complex perovskite ferroelectrics

Since these three MLCC samples have similar dimension and structure, the difference in ECE performance could be attributed to crystal structure and microstructure differences. Fig. 5a shows the XRD patterns of these three compositions. It can be observed that all the three samples have the perovskite structure, but PST has sharp superlattice diffraction peaks of ($^1/_2$ $^1/_2$ $^1/_2$) and ($^3/_2$ $^1/_2$ $^1/_2$) due to the long-range ordering of B-site atoms. The degree of order can be calculated by scaling the intensity I_o of the ($^1/_2$ $^1/_2$ $^1/_2$) supercell reflection to the inten-

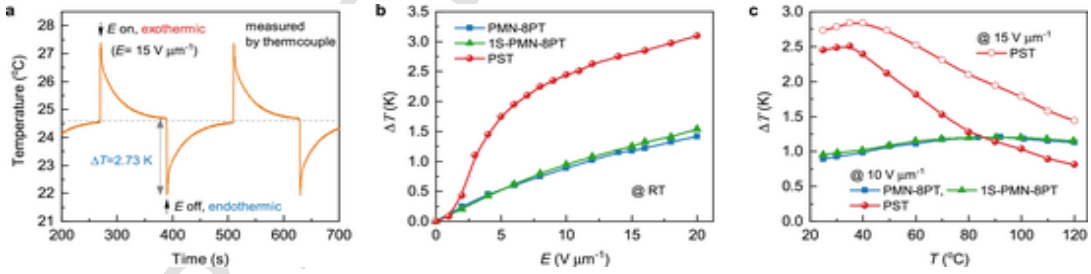

Fig. 3. EC temperature change with electric field and temperature. (a) A typical EC spectrum measured by thermocouple, the temperature change ΔT of PST MLCCs under 15 V μm^{-1}. A subsequent return to the starting temperature implies negligible Joule heating. (b) Adiabatic EC temperature change ΔT of PMN-8PT, 1S-PMN-8PT and PST MLCCs under different electric field at room temperature. (c) Adiabatic ECE temperature change ΔT of PMN-8PT, 1S-PMN-8PT and PST MLCCs under 15 V μm^{-1} at different temperature.

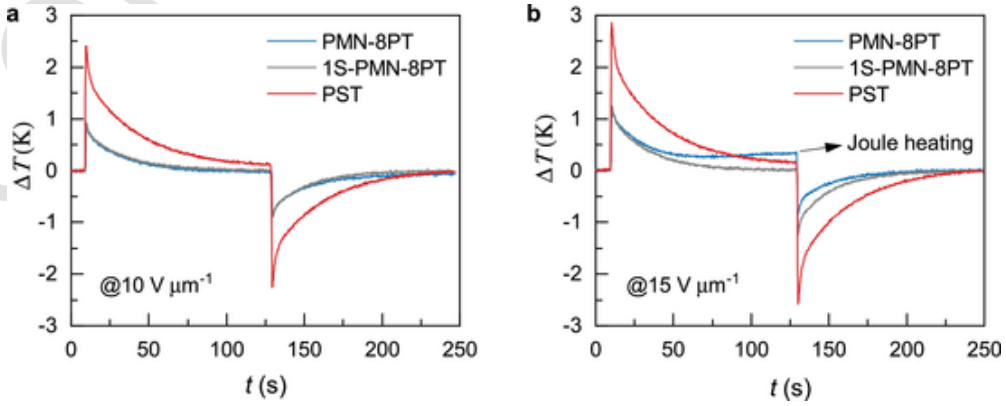

Fig. 4. EC temperature change ΔT versus time t of PMN-8PT, 1S-PMN-8PT and PST MLCCs at (a) 10 V μm^{-1} and b) 15 V μm^{-1}. The field were alternately applied and removed at ~2 min. intervals.

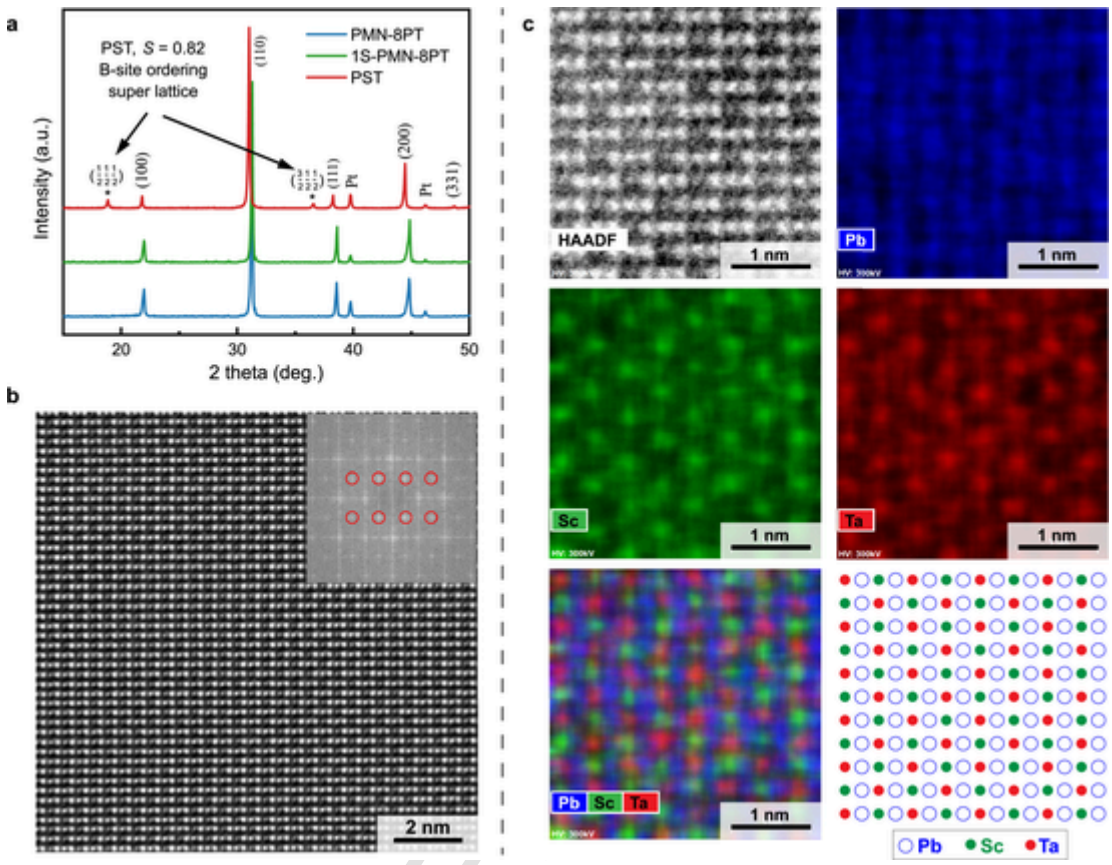

Fig. 5. (a) XRD patterns of PMN-8PT, 1S-PMN-8PT and PST MLCCs. (b) HRTEM image of PST. Inset image is the inverse Fourier transform of the HRTEM. (c) The atomic resolution energy-dispersive X-ray spectroscopy (EDS) mappings of Pb, Sc and Ta elements, and the overlapping mapping of the three elements above. The HRTEM and EDS images were taken along the [110] zone axis.

sity I_{100} of the (001) parent-lattice reflection of the perovskite [26]. The ordering parameter S was calculated using the equation $S = [(I_o/I_{100})_{observed}/(I_o/I_{100})_{calculated}]^{1/2}$. For completely ordered material of $S = 1$, (I_o/I_{100}) is 1.33. In this study, PST sintered at 1300 °C for 2 h has S of 0.82, whereas PMN-PT and 1S-PMN-PT have no long-range ordering.

In order to investigate the chemical ordering in PST, an atomic resolution HRTEM image was captured as shown in Fig. 5b. The Fourier transform pattern is presented as an inset. Superlattice diffraction spots are observed and marked by circles. In order to investigate the B-site chemical ordering, atomic resolution EDS was utilized. The EDS mappings of Pb, *Sc* and Ta ions taken along the [110] zone axis are displayed in Fig. 5c. It can be observed that the *Sc* and Ta ions occupy every second nearest neighbor of the B sites.

It has been reported that the ordered regions in PMN have a size of 2–5 nm, [27,28] the superlattice reflection cannot be detected by conventional X-ray diffraction. The superlattice diffraction peaks in PST from XRD indicates that the size of the ordered regions in PST is much larger than that of PMN-PT. The dark-field (DF) images of PMN-PT and PST were acquired using the ($^1/_2$ $^1/_2$ $^1/_2$) and (001) reflections, as shown in Fig. 6a and Fig. 6b, respectively. It is found that the DF image for PMN-PT shows small white dots of ~5 nm distributed in the whole grain. In contrast, the DF image for PST shows the ordered regions with sizes on the order of 100 nm distributed in the grain. The SAED patterns with the $[1\bar{1}0]$ zone axis are shown in Fig. 6c and Fig. 6d, respectively. Very weak superlattice diffraction {$^1/_2$ $^1/_2$ $^1/_2$} [8] exists in the PMN-PT sample, while strong superlattice diffraction {$^1/_2$ $^1/_2$ $^1/_2$} exists in the PST sample. This information confirms that the PST has long range ordering while PMN-PT has short range ordering, which is consistent with XRD diffraction and dielectric relaxation results described earlier.

The large difference in the degree of order/disorder and the size of the ordered regions in PMN and PST can be attributed to the difference in compositional order-disorder phase transitions temperatures. The electrostatic and elastic energies of the structure are minimized in the ordered state due to the valence and ionic radii differences of the two cations on B-sites, while thermal motion will destroy the order above the order-disorder phase transition temperature. The ordering implies the site exchange between B$'$ and B$''$ cations via diffusion. It is a relaxation process with a nearly infinite characteristic time at very low temperatures, but it can be quite fast at high temperatures. The order-disorder phase transitions temperatures of PST and PMN are ~1500 °C and 950 °C, respectively [8,17,19]. As a result, PST sintered at a relatively high temperature of 1300 °C (below the order-disorder phase transition temperature of ~1500 °C) forms a high degree of order and large ordered regions, while the compositional disorder of PMN cannot be changed by any heat treatment because the relaxation time of ordering below the order-disorder phase transition temperature of 950 °C is too long.

3.5. Correlation between cation order/disorder and the electrocaloric effect

Fig. 7a shows the electric field dependence of $\Delta T/E$ for PMN-PT, 1S-PMN-PT and PST MLCCs. It can be observed that the curve for $\Delta T/E$ as a function of the electric field E for PST MLCCs can be divided into two regimes (low-field and high-field). The maximum $\Delta T/E$ of 0.37 K μm V^{-1} was achieved under a critical electric field of 3 V μm^{-1}. The maximum $\Delta T/E$ of PST is about 3 times as that of PMN-PT and 1S-PMN-PT. $\Delta T/E$ is usually called the electrocaloric strength which is a critical parameter for practical applications. The typical value of $\Delta T/E$ for ferroelectric ceramics near room temperature is in the range of 0.1

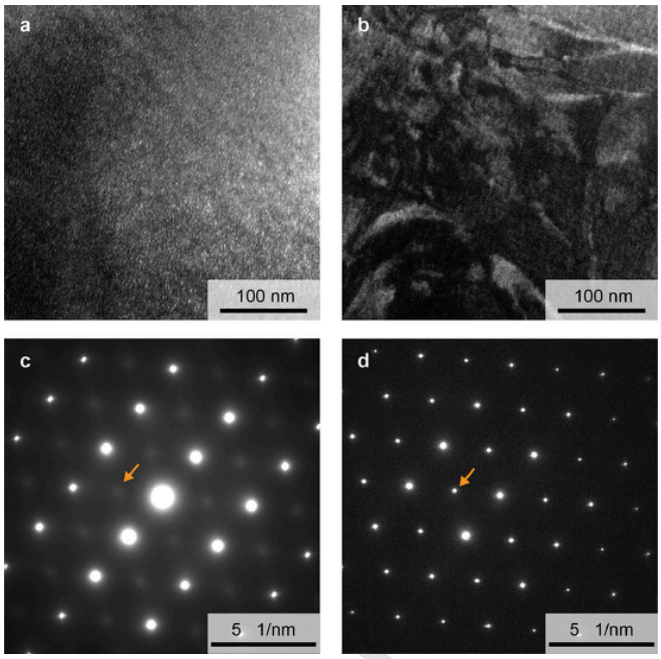

Fig. 6. (a) Dark field TEM image of PMN-PT using the reflection ($^1/_2\,^1/_2\,^1/_2$). (b) Dark field TEM image of PST using the reflection ($^1/_2\,^1/_2\,^1/_2$). The SAED patterns of (c) PMN-PT and d) PST, viewed along the $[1\,\bar{1}\,0]$ zone axis.

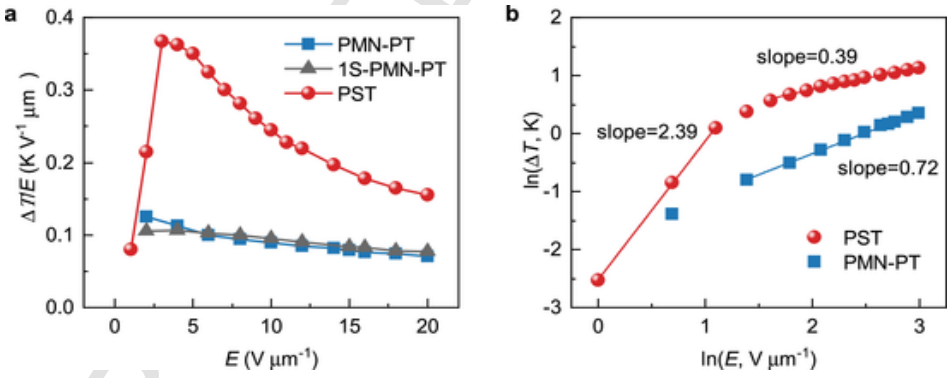

Fig. 7. (a) $\Delta T/E$ as a function of the electric field E. (b) $\ln(\Delta T)$ as a function of $\ln E$.

~0.6 K μm V $^{-1}$ [29]. Two regimes of $\Delta T/E$ have been observed in the [011] oriented PMN-PT single crystal [30]. Therefore, PMN-PT and 1S-PMN-PT MLCCs may also have two regimes, but the low-field regime for PMN-PT and 1S-PMN-PT MLCCs are narrow, and ΔT is very small.

To understand the difference in the ECE between PMN-PT and PST, a thermodynamic analysis is performed. Under constant pressure, the adiabatic change in temperature T is $dT = \frac{TdS}{C_P}$, where C_P is heat capacity. The entropy change caused by the change in electric field E is $dS = \left(\frac{\partial S}{\partial E}\right)_T dE$. Using the Maxwell relation $\left(\frac{\partial S}{\partial E}\right)_T = \left(\frac{\partial P}{\partial T}\right)_E$, where P is polarization, the entropy change becomes $dS = \left(\frac{\partial P}{\partial T}\right)_E dE$, and the temperature change becomes$dT = -\frac{T}{C_P}\left(\frac{\partial P}{\partial T}\right)_E dE$. The adiabatic temperature change caused by changing electric field from E_0 to E_1 is

$$\Delta T = -\int_{E_0}^{E_1} \frac{T}{C_P}\left(\frac{\partial P}{\partial T}\right)_E dE \approx -\frac{T}{C_P}\left(\frac{\partial P}{\partial T}\right)_E \Delta E, \tag{2}$$

where the approximation holds only if ΔE and ΔT are both small and T, C_P and $\left(\frac{\partial P}{\partial T}\right)_E$ remain approximately constant. Eq. (2) qualitatively explains the different EC behaviors of PMN-PT and PST. In order to achieve larger ΔT caused by the same ΔE, higher temperature T, larger value of $\left(\frac{\partial P}{\partial T}\right)_E$, and smaller heat capacity C_P are desired. Approximately the same C_P were assumed for PMN-PT and PST. According to the frequency dependence of dielectric constant in Fig. 2a, PST has weaker relaxor characteristics and PMN-PT has stronger relaxor characteristics. Since PST has weaker relaxor characteristics, it exhibits stronger temperature dependence as manifested in a narrower peak in ΔT~T curve (Fig. 3c). In contrast, PMN-PT has stronger relaxor characteristics and thus stronger diffuse phase transition characteristics, PMN-PT exhibits weaker temperature dependence as manifested in a broader peak in ΔT~T curve (Fig. 3c).

In order to further explore the physical origin of the two regimes and explain the different EC behaviors of PMN-PT and PST, Fig. 7(b) presents a log-log plot of ΔT vs E for the two materials. Fig. 7(b) reveals that at low electric fields, $\Delta T \propto E^2$, while at high fields, the two materi-

als display different E field dependences, i.e., $\Delta T \propto E^{2/5}$ for PST and $\Delta T \propto E^{2/3}$for PMN-PT. From the Landau-Devonshire phenomenological theory of ferroelectrics, assuming the projection of polarization on the field direction P, the free energy in the general form is formulated as [31]

$$G = -EP + g_0 + \frac{1}{2}g_2P^2 + \frac{1}{4}g_4P^4 + \frac{1}{6}g_6P^6 + ..., \tag{3}$$

In ferroelectrics, $g_2 = \alpha\left(T - T_0\right)$, where T_0 is the Curie-Weiss temperature and α>0. g_4 and g_6 are temperature-independent phenomenological coefficients; here $g_4 = \beta$ and $g_6 = \gamma$. The relationship between E and P is given by

$$E = \alpha\left(T - T_0\right)P + \beta P^3 + \gamma P^5. \tag{4}$$

Because of the absence of long-range ferroelectric order in zero field, the entropy as well as the temperature change can be obtained as

$$S = -\frac{\partial G}{\partial T} = -\frac{1}{2}\alpha P^2, \tag{5}$$

$$\Delta T = \frac{\alpha T}{2C_E}P^2. \tag{6}$$

For the first-order phase transition, $\boldsymbol{\beta}$<0, and $\boldsymbol{g}_6$ must be retained and taken as positive. Therefore, the relation between $\Delta \boldsymbol{T}$ and E is:

$$\frac{a}{k^{1/2}}\Delta T^{1/2} + \frac{b}{k^{3/2}}\Delta T^{3/2} + \frac{c}{k^{5/2}}\Delta T^{5/2} = E, \tag{7}$$

where $\boldsymbol{k} = \boldsymbol{\alpha T}/2\boldsymbol{C_E}$, $\boldsymbol{a} = \boldsymbol{\alpha}\left(\boldsymbol{T} - \boldsymbol{T}_0\right)$, $\boldsymbol{b} = \boldsymbol{\beta}$ and $\boldsymbol{c} = \boldsymbol{\gamma}$. For low electric field E, it can be approximated as $\Delta \boldsymbol{T} \propto \boldsymbol{E}^2$, while for high electric field, $\Delta \boldsymbol{T} \propto \boldsymbol{E}^{2/5}$.

For the second-order phase transition, $\boldsymbol{\beta}$>0, and $\boldsymbol{g}_6$ and higher order terms can be neglected. Therefore, relation between $\Delta \boldsymbol{T}$ and E is: [30,32,33]

$$\frac{a}{k^{1/2}}\Delta T^{1/2} + \frac{b}{k^{3/2}}\Delta T^{3/2} = E. \tag{8}$$

For low electric field E, it can be approximated as $\Delta \boldsymbol{T} \propto \boldsymbol{E}^2$, which is the same with the first-order transition. For high electric field, it reveals a different behavior, $\Delta \boldsymbol{T} \propto \boldsymbol{E}^{2/3}$.

As shown in Ref [34], the transition of relaxor to normal ferroelectric can be either first-order or second-order. The experimental results in Fig. 7(b) suggest that the EC response of PST follows the first-order phase transition behavior, i.e., $\Delta \boldsymbol{T} \propto \boldsymbol{E}^{2/5}$ at high fields, due to the ordering of B-site cations, while for PMN-PT, the high field EC behavior follows the second-order phase transition behavior, i.e., $\Delta \boldsymbol{T} \propto \boldsymbol{E}^{2/3}$.

These theoretical analyses are in good agreement with experimental observations as shown in Fig. 7b. However, it is noted that the low-field regime of PMN-PT relaxor is much narrower than that of PST, because the existence of random fields diminishes the ECE [35,36]. Ma et al. investigated the ECE in ferroelectrics and relaxor ferroelectrics using lattice-based Monte Carlo simulations [35]. It was found that with increase in the strength or the density of the random fields, the ECE peak shifts to a lower temperature but the ECE temperature change $\Delta \boldsymbol{T}$ is reduced. The simulation results imply that the presence of random fields reduces the entropy variation in an ECE cycle by pinning local polarization.

For PMN-PT, the polarization does not change significantly upon the application or removal of electric fields due to the random fields, so that the entropy does not change significantly either. Experimentally, increasing the ordering of PST via heat treatment or annealing can result in the transition of relaxor ferroelectrics to normal ferroelectrics, and thereby result in the reduction of random field and increase of the ECE temperature change $\Delta \boldsymbol{T}$ [8]. Therefore, the sharp increase of ECE temperature change $\Delta \boldsymbol{T}$ with $\Delta \boldsymbol{T} \propto \boldsymbol{E}^2$ in a wide low-field regime for PST gives a much larger ECE $\Delta \boldsymbol{T}$ than that of PMN-PT. In high-field regime, although the slope (2/3) of PMN-PT is larger than PST (2/5), the ECE temperature change $\Delta \boldsymbol{T}$ of PMN-PT is difficult to surpass that of PST because the material is easy to breakdown or degrade rapidly under the very high field.

3.6. Phase-field simulation of electrocaloric effect in normal and relaxor ferroelectrics

To better elucidate the cation order/disorder effect on ECE, a phase-field model was adopted to examine the EC properties in normal and relaxor ferroelectric polycrystals, respectively. Unlike normal ferroelectrics, the signature of relaxor ferroelectrics is the existence of polar nanoregions (PNRs) [37]. In some materials, PNRs coexist with normal ferroelectric domains. In this study, $BaTiO_3$ (BTO) was chosen as the normal ferroelectric material and BTO + PNR as the relaxor ferroelectric material. To a certain extent, the amount of PNRs indicates the ordering degree in relaxor ferroelectrics. In the model of ferroelectric polycrystals, the grain structure is characterized by the rotation matrix field R(r) and the ferroelectric state is described by the polarization vector field P(r). The evolution of the polarization P(r,t) is characterized by the time-dependent Ginzburg-Landau equation

$$\frac{\partial \mathbf{P}(\mathbf{r},t)}{\partial t} = -L\frac{\delta F}{\delta \mathbf{P}(\mathbf{r},t)} + \xi(\mathbf{r},t), \tag{10}$$

where L is kinetic coefficient and $\xi(\mathbf{r},t)$ is the Gaussian-distributed Langevin noise term. The total free energy is

$$F = \int d^3r\left[f\left(R_{ij}P_j\right) + \frac{\beta}{2}\frac{\partial P_i}{\partial r_j}\frac{\partial P_i}{\partial r_j} - E_k^{ex}P_k\right] + \frac{1}{2}\int \frac{d^3k}{(2\pi)^3}\left[\frac{n_in_j}{\varepsilon_0}\widetilde{P}_i\widetilde{P}_j^* + K_{ijkl}\widetilde{\varepsilon}_{ij}^{0}\widetilde{\varepsilon}_{kl}^{0\,*}\right], \tag{11}$$

where the Landau-Ginzburg-Devonshire (LGD) free energy is

$$f(\mathbf{P}) = \alpha_1\left(P_1^2 + P_2^2 + P_3^2\right) + \alpha_{11}\left(P_1^4 + P_2^4 + P_3^4\right) + \alpha_{12}\left(P_1^2P_2^2 + P_2^2\right) + \alpha_{111}\left(P_1^6 + P_2^6 + P_3^6\right) + \alpha_{112}\left[P_1^4\left(P_2^2 + P_3^2\right) + P_2^4\left(P_3^2 + P_1^2\right) + \right] + \alpha_{123}P_1^2P_2^2P_3^2$$

More details on the phase-field models of ferroelectric polycrystals can be found in Ref [38]. Therefore, the following LGD coefficients were adopted in the phase-field simulations: α_1 = 3.34(T-381)×10^5 m/F, α_{11} = 4.69(T-393)×10^6 – 2.02×10^8 m^5/C^2F, α_{12} = 3.23×10^8 m^5/C^2F, α_{111} = −5.52(T-393)×10^7 + 2.76×10^9 m^9/C^4F, α_{112} = 4.47×10^9 m^9/C^4F, α_{123} = 4.91×10^9 m^9/C^4F for the ferroelectrics $BaTiO_3$ [39]; α_1 = 7.014×10^7 m/F, α_{11} = −2.8893×10^9 m^5/C^2F, α_{12} = 4.845×10^9 m^5/C^2F, α_{111} = 3.9744×10^{10} m^9/C^4F, α_{112} = 6.705×10^{10} m^9/C^4F, α_{123} = 7.365×10^{10} m^9/C^4F for the local polar regions. The electrostrictive coefficients are Q_{11} = 0.11 m^4C^{-2}, Q_{12} = −0.045 m^4C^{-2}, and Q_{44} = 0.029 m^4C^{-2}. These LDG coefficients correspond to a Curie temperature for ferroelectric BTO of 120 °C, i.e. they underpredict the actual Curie temperature for pure material.

Fig. 8 shows the simulated domain structures of paraelectric BTO and relaxor ferroelectric BTO + PNR polycrystals at electric fields of 0 and 2 V μm^{-1} along the z-direction. There is no net polarization for BTO at zero electric field and 395 K (above the Curie temperature) as shown in Fig. 8(a). As expected, an external electric field induces a ferroelectric phase and an ordered domain state, and the polarization forms multiple domains, as shown in Fig. 8(b,c). Since the electric field is applied along z-direction, the induced polarization is predominantly parallel to the field and thus the domain structure becomes less evident. For the relaxor ferroelectrics, however, the existence of PNRs may result in disordered domains at the same temperature. In the sim-

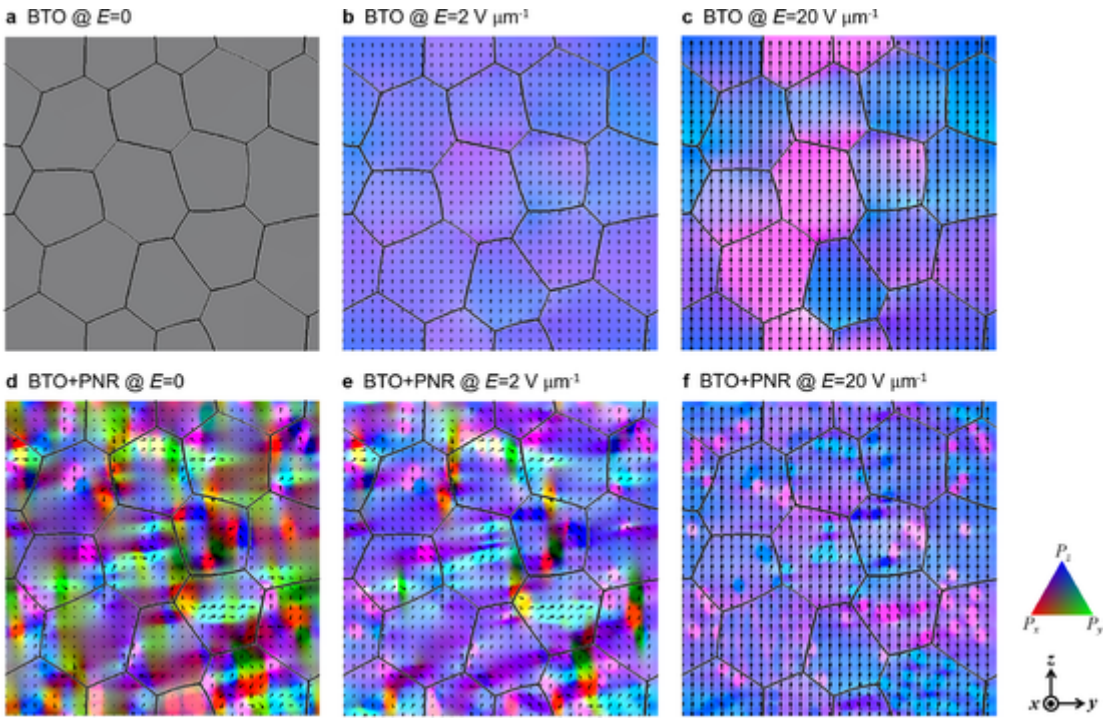

Fig. 8. Simulated domain structures of BTO and BTO + PNR polycrystals under electric fields of 0, 2 and 20 V μm^{-1} at 395 K.

ulations, the size of PNRs is ~4 nm and the volume fraction of these local polar regions is ~10%. Unlike the normal ferroelectrics whose net polarizations vanish above the Curie temperature, the local polar regions in relaxor ferroelectrics may still exhibit a ferroelectric-like phase at the same temperature even at zero electric field, given that the paraelectric BTO matrix is slightly polarized by the random field generated from the PNR, as shown in Fig. 8(c). Under an electric field of 2 V μm^{-1}, the domains are reoriented toward the *z*-direction and the polarizations in BTO matrix also enhanced as shown in Fig. 8(d). Under a moderate electric field of 2 V μm^{-1}, the polarization in the BTO matrix is slightly enhanced and reoriented toward the *z*-direction, while the polarization of the PNRs is not significantly impacted since the electric field is not strong enough to switch all the polarization orientations of the PNRs, as shown in Fig. 8(e). Under a large electric field of 20 V μm^{-1}, the polarization in the BTO matrix is significantly enhanced and even the polarization in the PNRs is also reoriented toward the field direction, as shown in Fig. 8(f).

The simulated EC temperature change ΔT of BTO and BTO + PNR under different electric field at 395 K is shown in Fig. 9(a). The simulations reveal that the random field generated by local polar regions in this case reduce the EC temperature change ΔT, which is in good agreement with the experimental observations in Fig. 3(b) as well as the lattice-based Monte Carlo simulations [35]. These findings indicate that the EC temperature change can be further reduced if the volume fraction of PNRs in relaxor ferroelectrics is elevated, which is consistent with the experimental observations on PST, i.e., the ECE of PST is reduced with increasing disorder [40,41]. To better elucidate the EC behavior, these simulated data are replotted using a logarithmic scale, as shown in Fig. 9(b). As expected, the two-regime feature emerges again. In the low-field regime, since the polarization changes almost linearly with electric field while ΔT is proportional to the square of polarization according to Eq. (6), the EC temperature change ΔT increases quadratically with electric field as $\Delta T \propto E^2$ for both normal and relaxor ferroelectrics, which is in good agreement with the theoretical analysis in Sec. 2.5. In the high-field regime, the polarization under electric field manifests a nonlinear behavior that is modulated by different higher-order terms, thereby normal and relaxor ferroelectrics would exhibit different EC behaviors. For the relaxor ferroeletrics, the high-field slope

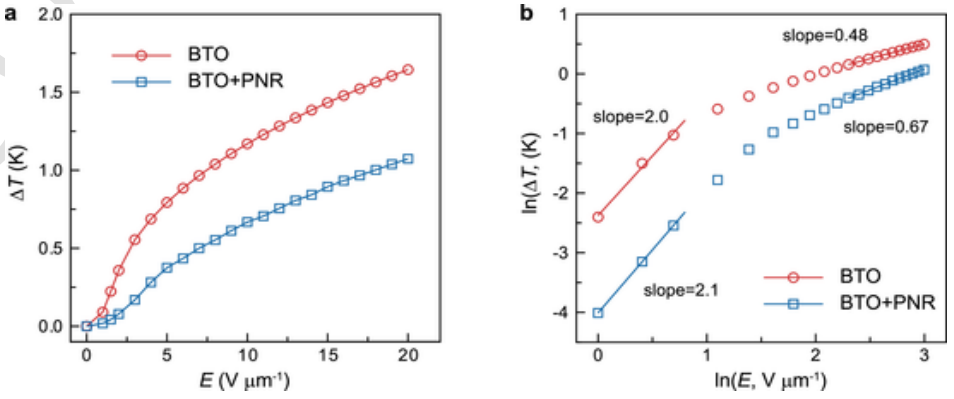

Fig. 9. (a) Simulated ECE temperature change ΔT of BTO and BTO + PNR under different electric field at 395 *K*. (b) Logarithmic replotting of simulated data in (a).

is 0.67, indicating $\Delta T \propto E^{2/3}$, which is attributed to the second-order phase transition, as discussed in Section 2.5. For the normal ferroelectrics, the high-field slope is 0.48 that is slightly larger than the theorectial value 2/5. In fact, the simulations show that if the electric field is further increased, the slope will continuously decrease to approach 2/5. This implies that unless the electric field is sufficiently high, the slope value will be between 2/5 and 2/3, i.e., the β-term in Eq. (8) is not negligible as compared to the γ-term when the field is not sufficiently high. Nevertheless, whether a field is high enough, is not merely determined by the field magnitude, because the specific ferroelectric material as well as its mircrostructure also plays an important role. Thus, the conclusion made by phase-field simulations on the correlation between cation order/disorder and ECE coincides with the experimental observations and theorectial analysis.

4. Conclusions

In summary, PST, PMN-8PT and 1S-PMN-PT MLCCs with comparable structural configuration were fabricated and their EC properties were characterized. The EC temperature change ΔT of PMN-8PT, 1S-PMN-8PT and PST MLCCs under 20 V μm^{-1} reach to 1.42 K, 1.54 K, and 3.10 K, respectively. Theoretical analysis was carried out to elucidate the different EC behaviors performed by PMN-PT and PST. The analysis reveals that in the low-field regime, the EC temperature change behaves as $\Delta T \propto E^2$ for both PMN-PT and PST, while in the high-field regime, the EC temperature change follows $\Delta T \propto E^{2/3}$ for PMN-PT and $\Delta T \propto E^{2/5}$ for PST. Phase-field simulations were performed to better elucidate the cation order/disorder effect on ECE at the domain level, which reveal that the random field generated by local polar regions associated with the B-site disordering in relaxors reduces the EC temperature change, indicating that the B-site ordering is desired for improved ECE in relaxor ferroelectrics.

Declaration of Competing Interest

The authors declare that they have no known competing financial interests or personal relationships that could have appeared to influence the work reported in this paper.

Acknowledgements

This material is based upon work supported by the center for 3D Ferroelectric Microelectronics (3DFeM), an Energy Frontier Research Center funded by the U.S. Department of Energy, Office of Science, Office of Basic Energy Sciences Energy Frontier Research Centers program under Award Number DE-SC0021118. B.P. acknowledges the financial support from Center for Energy Harvesting Materials and Systems. Y.Y and L.G. contributed equially to this work. We thank Dr. Haiying Wang and Dr. Ke Wang for TEM sample preparation and characterization. All microscopy work was performed at the Penn State Materials Characterization Laboratory.

References

[1] M. Valant, Electrocaloric materials for future solid-state refrigeration technologies, Prog. Mater. Sci. 57 (6) (2012) 980–1009.
[2] J.Y. Shi, D.L. Han, Z.C. Li, L. Yang, S.G. Lu, Z.F. Zhong, J.P. Chen, Q.M. Zhang, X.S. Qian, Electrocaloric cooling materials and devices for zero-global-warming-potential, high-efficiency refrigeration, Joule 3 (5) (2019) 1200–1225.
[3] X. Moya, S. Kar-Narayan, N.D. Mathur, Caloric materials near ferroic phase transitions, Nat. Mater. 13 (5) (2014) 439–450.
[4] B. Lu, X. Jian, X. Lin, Y. Yao, T. Tao, B. Liang, H. Luo, S.G. Lu, Enhanced electrocaloric effect in 0.73Pb($Mg_{1/3}Nb_{2/3}$)O_3-0.27$PbTiO_3$ single crystals via direct measurement, Crystal 10 (6) (2020) 451.
[5] A.S. Mischenko, Q. Zhang, J.F. Scott, R.W. Whatmore, N.D. Mathur, Giant electrocaloric effect in thin-film $PbZr_{0.95}Ti_{0.05}O_3$, Science 311 (5765) (2006) 1270–1271.
[6] B. Neese, B.J. Chu, S.G. Lu, Y. Wang, E. Furman, Q.M. Zhang, Large electrocaloric effect in ferroelectric polymers near room temperature, Science 321 (5890) (2008) 821–823.
[7] S. Kar-Narayan, N.D. Mathur, Predicted cooling powers for multilayer capacitors based on various electrocaloric and electrode materials, Appl. Phys. Lett. 95 (24) (2009) 242903.
[8] B. Nair, T. Usui, S. Crossley, S. Kurdi, G.G. Guzman-Verri, X. Moya, S. Hirose, N.D. Mathur, Large electrocaloric effects in oxide multilayer capacitors over a wide temperature range, Nature 575 (7783) (2019) 468–472.
[9] C. Molin, J. Perantie, F.Le Goupil, F. Weyland, M. Sanlialp, N. Stingelin, N. Novak, D.C. Lupascu, S. Gebhardt, Comparison of direct electrocaloric characterization methods exemplified by 0.92 Pb($Mg_{1/3}Nb_{2/3}$)O_3-0.08 $PbTiO_3$ multilayer ceramics, J. Am. Ceram. Soc. 100 (7) (2017) 2885–2892.
[10] T. Usui, S. Hirose, A. Ando, S. Crossley, B. Nair, X. Moya, N.D. Mathur, Effect of inactive volume on thermocouple measurements of electrocaloric temperature change in multilayer capacitors of 0.9 Pb($Mg_{1/3}Nb_{2/3}$)O_3-0.1$PbTiO_3$, J. Phys. D Appl. Phys. 50 (42) (2017) 424002.
[11] A. Torello, P. Lheritier, T. Usui, Y. Nouchokgwe, M. Gerard, O. Bouton, S. Hirose, E. Defay, Giant temperature span in electrocaloric regenerator, Science 370 (6512) (2020) 125–129.
[12] Y.D. Wang, Z.Y. Zhang, T. Usui, M. Benedict, S. Hirose, J. Lee, J. Kalb, D. Schwartz, A high-performance solid-state electrocaloric cooling system, Science 370 (6512) (2020) 129–133.
[13] Y. Liu, J.F. Scott, B. Dkhil, Direct and indirect measurements on electrocaloric effect: recent developments and perspectives, Appl. Phys. Rev. 3 (3) (2016) 031102.
[14] Z.G. Ye, Relaxor Ferroelectric Complex perovskites: structure, properties and phase transitions, Key Eng. Mater. 155–156 (1998) 81–122.
[15] A.A. Bokov, Z.G. Ye, Recent progress in relaxor ferroelectrics with perovskite structure, J. Mater. Sci. 41 (1) (2006) 31–52.
[16] P.K. Davies, M.A. Akbas, Chemical order in PMN-related relaxors: structure, stability, modification, and impact on properties, J. Phys. Chem. Solids 61 (2) (2000) 159–166.
[17] L. Farber, M. Valant, M.A. Akbas, P.K. Davies, Cation ordering in Pb($Mg_{1/3}Nb_{2/3}$)O_3-Pb($Sc_{1/2}Nb_{1/2}$)O_3 (PMN-PSN) solid solutions, J. Am. Ceram. Soc. 85 (9) (2002) 2319–2324.
[18] N. Setter, L.E. Cross, The role of B-site cation disorder in diffuse phase-transition behavior of perovskite ferroelectrics, J. Appl. Phys. 51 (8) (1980) 4356–4360.
[19] C.G.F. Stenger, A.J. Burggraaf, Order-disorder reactions in the ferroelectric perovskites Pb($Sc_{1/2}Nb_{1/2}$)O_3 and Pb($Sc_{1/2}Ta_{1/2}$)O_3 .1. kinetics of the ordering process, Phys. Status Solidi A 61 (1) (1980) 275–285.
[20] C.G.F. Stenger, A.J. Burggraaf, Order-disorder reaction in the ferroelectric perovskites Pb($Sc_{1/2}Nb_{1/2}$)O_3 and Pb($Sc_{1/2}Ta_{1/2}$)O_3 .2. relation between ordering and properties, Phys. Status Solidi A 61 (2) (1980) 653–664.
[21] Z. Fang, X. Jiang, X. Tian, F. Zheng, M. Cheng, E. Zhao, W. Ye, Y. Qin, Y. Zhang, Ultratransparent PMN-PT electro-optic ceramics and its application in optical communication, Adv. Opt. Mater. 9 (13) (2021) 2002139.
[22] C.C. Li, B. Xu, D.B. Lin, S.J. Zhang, L. Bellaiche, T.R. Shrout, F. Li, Atomic-scale origin of ultrahigh piezoelectricity in samarium-doped PMN-PT ceramics, Phys. Rev. B 101 (14) (2020) 140102(R).
[23] C.G.F. Stenger, F.L. Scholten, A.J. Burggraaf, Ordering and diffuse phase-transitions in Pb($Sc_{1/2}Ta_{1/2}$)O_3 Ceramics, Solid State Commun. 32 (11) (1979) 989–992.
[24] Y.N. Huang, Y.N. Wang, H.M. Shen, Internal-friction and dielectric loss related to domain-walls, Phys. Rev. B 46 (6) (1992) 3290–3295.
[25] D.B. Lin, Z.R. Li, F. Li, S.J. Zhang, Direct observation of domain wall motion and novel dielectric loss in 0.23Pb($In_{1/2}Nb_{1/2}$)O_3-0.42Pb($Mg_{1/3}Nb_{2/3}$)O_3-0.35$PbTiO_3$ crystals, Crystengcomm 15 (32) (2013) 6292–6296.
[26] H.C. Wang, W.A. Schulze, Order-disorder phenomenon in lead scandium tantalate, J. Am. Ceram. Soc. 73 (5) (1990) 1228–1234.
[27] C. Boulesteix, F. Varnier, A. Llebaria, E. Husson, Numerical determination of the local ordering of Pb($Mg_{1/3}Nb_{2/3}$)O_3 from high-resolution electron-microscopy images, J. Solid State Chem. 108 (1994) 141–147.
[28] M. Yoshida, S. Mori, N. Yamamoto, Y. Uesu, J.M. Kiat, TEM observation of polar domains in relaxor ferroelectric Pb($Mg_{1/3}Nb_{2/3}$)O_3, Ferroelectrics 217 (1–4) (1998) 327–333.
[29] S.G. Lu, X. Lin, J. Li, D. Li, Y. Yao, T. Tao, B. Liang, Enhanced electrocaloric strengths at room temperature in (Sr_xBa_{1-x})($Sn_{0.05}Ti_{0.95}$)O_3 lead-free ceramics, J. Alloy Compd. 871 (2021) 159519.
[30] S.G. Lu, Z.H. Cai, Y.X. Ouyang, Y.M. Deng, S.J. Zhang, Q.M. Zhang, Electrical

field dependence of electrocaloric effect in relaxor ferroelectrics, Ceram. Int. 41 (2015) S15–S18.
[31] M.E. Lines, A.M. Glass, Principles and Applications of Ferroelectrics and Related Materials, Oxford University Press, 2001.
[32] S.G. Lu, Q. Zhang, Large electrocaloric effect in relaxor ferroelectrics, J. Adv. Dielectr. 2 (3) (2012) 1230011.
[33] S.G. Lu, B. Rozic, Q.M. Zhang, Z. Kutnjak, R. Pirc, Electrocaloric effect in ferroelectric polymers, Appl. Phys. A 107 (3) (2012) 559–566.
[34] R. Pirc, Z. Kutnjak, R. Blinc, Q.M. Zhang, Electrocaloric effect in relaxor ferroelectrics, J. Appl. Phys. 110 (7) (2011).
[35] Y.B. Ma, K. Albe, B.X. Xu, Lattice-based Monte Carlo simulations of the electrocaloric effect in ferroelectrics and relaxor ferroelectrics, Phys. Rev. B 91 (18) (2015) 184108.
[36] G.G. Guzman-Verri, P.B. Littlewood, Why is the electrocaloric effect so small in ferroelectrics? APL Mater. 4 (6) (2016) 064106.
[37] F. Li, S.J. Zhang, T.N. Yang, Z. Xu, N. Zhang, G. Liu, J.J. Wang, J.L. Wang, Z.X. Cheng, Z.G. Ye, J. Luo, T.R. Shrout, L.Q. Chen, The origin of ultrahigh piezoelectricity in relaxor-ferroelectric solid solution crystals, Nat. Commun. 7 (2016) 13807.
[38] Y. Yan, L.D. Geng, L.F. Zhu, H. Leng, X. Li, H. Liu, D. Lin, K. Wang, Y.U. Wang, S. Priya, Ultrahigh piezoelectric performance through synergistic compositional and microstructural engineering, Adv. Sci. 9 (14) (2022) 2105715.
[39] A.J. Bell, Phenomenologically derived electric field-temperature phase diagrams and piezoelectric coefficients for single crystal barium titanate under fields along different axes, J. Appl. Phys. 89 (7) (2001) 3907–3914.
[40] L. Shebanovs, A. Sternberg, W.N. Lawless, K. Borman, Isomorphous ion substitutions and order-disorder phenomena in highly electrocaloric lead-scandium tantalate solid solutions, Ferroelectrics 184 (1996) 239–242.
[41] L. Shebanovs, K. Borman, W.N. Lawless, A. Kalvane, Electrocaloric effect in some perovskite ferroelectric ceramics and multilayer capacitors, Ferroelectrics 273 (2002) 2515–2520.